Advance Publication

IEEJ Journal of Industry Applications
J-STAGE Advance published date : July 25, 2025
DOI : 10.1541/ieejjia.25000120

Paper

Adaptive One Sample Ahead Preview Control with Multilevel Validation for Non-Sinusoidal PMSMs in *dq* Coordinates

Guilherme Vieira Hollweg[*a)] Non-member, Lucas Rossato Rocha[**] Non-member
Van-Hai Bui[*] Non-member, Rodrigo Padilha Vieira[**] Non-member
Mengqi Wang[*] Non-member, Wencong Su[*] Non-member

(Manuscript received January 05, 2025, revised xxxx xy, 2025)

This study shows the design and implementation of an adaptive one sample ahead preview (AOSAP) control structure tailored for non-sinusoidal permanent magnet synchronous motors (PMSMs), implemented in both *d* and *q* coordinates. The control strategy employs a first-order reference model and is systematically compared against conventional Proportional-Integral (PI) controllers. The simulation results in Matlab and the experimental evaluations conducted on a Typhoon hardware-in-the-loop (HIL) 604 platform and a physical prototype demonstrate the superior performance of the proposed AOSAP controller. It exhibits lower tracking errors and faster regulation compared to classical PI controllers. The control algorithms are developed on Texas Instruments Delfino C2000 microcontrollers, showcasing the feasibility of the proposed approach in real world applications.

Keywords: PMSM, robustness, RMRAC-based, AOSAP, non-linear control, direct adaptive control.

1. Introduction

The demand for electric vehicles (EVs) has drastically increased in the past few years due to growing concerns regarding green technologies and the reduction of fossil fuel consumption [2–4]. In response to this trend, the fields of power electronics, electric machines, power drives, and those related to electrification and transportation have also experienced significant growth and development [5–7].

Permanent magnet synchronous machines (PMSMs) are crucial components regarding electric traction, finding widespread applications in diverse sectors, ranging from wind power to electric vehicles [8–12]. These machines leverage permanent magnets in their rotor design, contributing to their efficiency and high power density [13]. A non-sinusoidal PMSM deviates from the traditional sinusoidal back electromotive force (EMF) waveform commonly associated with synchronous motors. This deviation is achieved through intentional motor design or control strategies, resulting in waveforms such as trapezoidal or square [14]. Advantages of non-sinusoidal PMSMs include simplified control algorithms and potentially reduced manufacturing costs [15]. However, they may exhibit drawbacks, such as increased torque ripple and higher harmonics in motor currents, affecting smoothness of operation and introducing additional losses [16]. The choice between sinusoidal and non-sinusoidal PMSMs depends on the specific application requirements, with non-sinusoidal designs often favored in cost-effective and simpler control-oriented applications.

Over the past decades, significant advancements have been made in control methodologies for non-sinusoidal PMSMs. Conventional proportional-integral (PI) controllers are widely adopted due to their simplicity and ease of implementation, but they may struggle to meet the stringent performance requirements of modern applications. In this context, several novel control strategies have emerged to deal with non-sinusoidal PMSMs [17]. Among the proposed structures, there are predictive controllers [18–20], resonant controllers [21, 22], sliding mode controllers [23], direct injection of current harmonics [24–26], artificial neural networks [27], linear quadratic regulators [28], deadbeat [29], active disturbance rejection [30] and others. However, all these aforementioned control structures have something in common: they lack of real-time adaptability. In this regard, adaptive control techniques have gained traction in recent years as promising solutions for power electronics and motor drives applications. This paper proposes the application of an adaptive one sample ahead preview (AOSAP) controller for non-sinusoidal PMSMs in order to improve performance. This control structure is possible to be implemented in both *dq* coordinates (or only for the *q* coordinate) and is based on robust adaptive control theory. In this sense, it employs a reference model for dictating the controlled signal's behavior and adapting the $\boldsymbol{\theta}$ vector (the adaptive gains linked to the internal signals of the system) to achieve low tracking error. Furthermore, by working with one sample ahead, it tends to present fast regulation performance in exchange for some overshoot, which can be managed by an appropriately designed refer-

a) This paper is based on Reference [1], which is published in ICEMS 2024 (c) 2024 IEEJ.

Correspondence to: (hollweg,wencong)@umich.edu
[*] Department of Electrical and Computer Engineering (ECE), University of Michigan-Dearborn, 4901 Evergreen Road, Dearborn, MI, 48128, USA.
[**] Power Electronics and Control Group, Federal University of Santa Maria, Av. Roraima, 1000, Predio 7, Centro de Tecnologia, Santa Maria, RS, Brazil.

ence model and tuning gains.

The contributions of this research can be described as follows:

- The AOSAP control strategy is applied for non-sinusoidal PMSMs, aiming for improved performance, built upon the foundation of robust model reference adaptive control (RMRAC) theory. This control approach is designed to deliver rapid regulation performance, leveraging the characteristics of the Deadbeat controller while incorporating the robustness inherent in model reference adaptive control (MRAC). This combination ensures fast and reliable system response under varying operating conditions.
- The controller is implemented in the d and q coordinates (or only for the q coordinate). Moreover, the validation of the control method is first carried out in Matlab, and later in a control-hardware-in-the-loop (C-HIL), implemented in a Delfino C-2000 digital signal processor (DSP). Later, the control structure was validated in a prototype. In this regard, the discrete-time control architecture is validated in a real environment in terms of control, and a comparative analysis reveals a significant improvement compared to conventional PI controllers.

The structure of this paper unfolds as follows: Section II outlines the mathematical formulation of the control problem, while Section III delves into the design of the AOSAP controller. Moving on, Section IV presents the feasibility of the control structure to regulate the plant in a Matlab environment. Section V presents the results obtained through C-HIL and provides a comparative analysis with a traditional structure. Section VI presents experimental results, validating the control method in a real scenario. Finally, Section VII offers concluding remarks for this study.

2. Non-Sinusoidal PMSM Mathematical Model

For modeling the electrical machine in the synchronous reference frame dq, there is

$$\begin{aligned} v_q(t) &= R_s i_q(t) + \omega_e L_s i_d(t) + L_s \frac{d}{dt} i_q(t) + e_q(t), \\ v_d(t) &= R_s i_d(t) - \omega_e L_s i_q(t) + L_s \frac{d}{dt} i_d(t) + e_d(t), \end{aligned} \tag{1}$$

where v_d, v_q represent the dq voltages, i_d, i_q are the stator currents, e_d, e_q denote the back-EMF, R_s is the resistance to the stator, L_s is the inductance, and ω_e is the synchronous speed. From (1), the back-EMF can be expressed as given in (2) for non-sinusoidal PMSM [31]:

$$\begin{aligned} e_d(t) &= E_q + \sum_h^\infty E_{q_h} \cos(h\omega_e t), \\ e_q(t) &= \sum_h^\infty E_{d_h} \sin(h\omega_e t), \end{aligned} \tag{2}$$

where E_q represents the constant component of e_q, E_{q_h} and E_{d_h} are the harmonic amplitudes, and $h = 6, 12, 18, \ldots$ denotes the harmonic order. Since the stator currents depend directly on the difference between the dq voltages and the back-EMF, i_d and i_q will exhibit the same behavior as depicted in (1). Consequently, the electromagnetic torque T_e will also exhibit a ripple, according to

$$\begin{aligned} T_e(t) = \frac{1}{\omega_r}\{e_d(t) i_d(t) + e_q(t) i_q(t)\} = \\ \frac{1}{\omega_r}\{T_0 + \sum_h^\infty T_h \cos(h\omega_e t)\}, \end{aligned} \tag{3}$$

where T_0 is the constant component of T_e, T_h is the harmonic amplitude and ω_r is the rotor speed.

Usually, the torque in a non-sinusoidal PMSM is modeled including a constant and an oscillatory component. If this is the case, the current references i_{dq} must also include an oscillatory + constant component [32] to compensate for torque ripple. However, if the back-EMF harmonics are not significant, the oscillatory component in (2) can be assumed to be a small disturbance, constant i_{dq} currents can be applied.

From (1), the transfer function that relates current and voltage can be obtained as

$$G_i(s) = \frac{i_{dq}}{v_{dq}} = \frac{1}{sL_s + R_s}. \tag{4}$$

The mechanical machine model is depicted in the following.

$$\frac{d}{dt}\omega_r(t) = -\frac{B_n}{J}\omega_r(t) + \frac{1}{J}(T_e(t) - T_L(t)), \tag{5}$$

where B_n represents the viscous friction coefficient, J denotes the moment of inertia, and T_L stands for the torque load. Taking the result from (5), the transfer function linking rotor speed and torque can be computed as follows

$$G_\omega(s) = \frac{\omega_r}{T_e} = \frac{1}{sJ + B_n}. \tag{6}$$

The machine parameters are depicted in Table 1. Detailed modeling can be found in [33].

Table 1: Machine parameters.

Parameter	Name	Value
V_{DC}	Voltage DC bus	72 V
P	Number of poles	32
J	Moment of inertia	0.0226 kgm^2
B_n	Viscous friction coefficient	0.0097 Nms
ω_{nom}	Nominal rotor speed	50 rad/s
L_s	Stator inductance	88.61 μH
R_s	Stator resistance	78.17 $m\Omega$

3. Controller Description

This section describes the AOSAP controller for the non-sinusoidal PMSM application. However, stability analysis using Lyapunov criteria will not be fully discussed in this paper, since it was shown in detail in [34]. Nevertheless, the appendix sections provide a brief description of the stability analysis and show the controllers' robustness to matched and unmatched dynamics.

3.1 Assumptions on Plant and Reference Model

Consider a general linear time-invariant single-input single-output (SISO) system as

$$G(z) = G_0(z)\left[1 + \mu_1 \Delta_m(z)\right] + \mu_2 \Delta_a(z). \tag{7}$$

Observe that there are two types of unmodeled dynamics: additive, denoted by $\mu_2\Delta_a(z)$, and multiplicative, represented

by $\mu_1\Delta_m(z)$. For simplicity, the same value of μ is assumed for unmodeled additive and multiplicative dynamics. Then, $\mu = \mu_1 = \mu_2$. In addition, the parameter μ is bounded in the interval $[0, \bar{\mu})$, with $\bar{\mu}$ being a positive real number.

Rewriting (7) as

$$G(z) = G_0(z)\mu\Delta G(z), \tag{8}$$

and

$$G_0(z) = k_p\frac{Z_o(z)}{R_o(z)}, \tag{9}$$

where $G_0(z)$ represents the nominal part of the plant. Also, k_p is a scalar gain, $Z_o(z)$ is the numerator, and $R_o(z)$ is the denominator. Then, $G_0(z)$ must satisfy the following assumptions:

A_I: k_p is an unknown gain, but its sign must be known.

A_{II}: $Z_o(z)$ is a monic polynomial, with order m, with all roots inside the unit radius circle.

A_{III}: $R_o(z)$ is a monic polynomial, with order n, where $n > m$.

A_{IV}: the coefficients of $Z_o(z)$ and $R_o(z)$ may be unknown.

Remark I: It is also important to emphasize that A_I ensures the proper initialization of θ_1 (showed in detail in next subsection), avoiding division by zero. This gain always has the opposite sign of k_p. Therefore, once the sign of k_p is known, θ_1 will not cross zero during its convergence.

The tracking error can be described as

$$e_1 = y - y_m, \tag{10}$$

where y and y_m are the outputs of the plant and reference model, respectively. Moreover, y_m is

$$y_m = W_m(z)r, \tag{11}$$

and r is a bounded reference signal, while $W_m(z)$ is the reference model transfer function, given by

$$W_m(z) = k_m\frac{1}{D_m(z)}, \tag{12}$$

where k_m is the gain and $D_m(z)$ is the transfer function denominator. Furthermore, $W_m(z)$ must satisfy the assumptions:

A_V: $D_m(z)$ is an n-order monic polynomial, with all roots inside the unit radius circle.

A_{VI}: k_m is a high-frequency gain constant, with the same sign as k_p.

Remark II: The reference model typically shares the same relative degree as the modeled part of the plant ($G_0(z)$) for the matching condition. In the control structure presented, the intentional choice of a first-order reference model ($W_m(z)$) allows the plant ($G(z)$) to have any order. This simplification is made with the understanding that the omitted dynamics have a minimal impact on the overall behavior of the system. The Lyapunov stability analysis presented in [34] and briefly discussed in the appendix further demonstrate the controller's robustness in handling both included and disregarded dynamics.

3.2 Control law As presented in Section II, the non-sinusoidal PMSM control problem consists in a first order system. Thus, be the plant modeled as

$$G_0(z) = \frac{b}{z-a} = \frac{y(z)}{u(z)}. \tag{13}$$

The dominant dynamics of the system are characterized by the parameters a and b. Moreover, let y denote the output of the plant and u represent the input to the plant. In addition, the reference model is

$$W_m(z) = \frac{b_{mr}}{z-a_{mr}} = \frac{y_m(z)}{r(z)}. \tag{14}$$

In this context, the characteristics of $W_m(z)$ are expressed by the parameters a_{mr} and b_{mr}, dictating its dominant dynamics. The output y_m of $W_m(z)$ is designed to follow the reference signal r. Ensuring the matching condition requires aligning the relative degree of the reference model with that of the nominal part of the plant, denoted as $G_0(z)$. Expressing (13) in a different way, there is

$$zy(z) - ay(z) = bu(z), \tag{15}$$

which, in its implementable form is

$$y(k+1) = ay(k) + bu(k). \tag{16}$$

It becomes essential to match the dynamics of the reference model with the regulated signal, ensuring $y(k+1) = y_m(k+1)$. Rephrasing (16), the entirety of the control action can be formulated as:

$$u(k) = \frac{y(k+1) - ay(k)}{b}. \tag{17}$$

Substituting $y(k+1)$ with $y_m(k+1)$ in (17), follows

$$u(k) = \frac{y_m(k+1) - a[ay(k-1) + bu(k-1)]}{b}. \tag{18}$$

Furthermore, from (14), it also follows

$$y_m(k+1) = a_{mr}y_m(k) + b_{mr}r(k), \tag{19}$$

which can be rewritten in its implementable form by shifting the (k) operators, as

$$y_m(k) = a_{mr}y_m(k-1) + b_{mr}r(k-1). \tag{20}$$

To obtain the control action, replace (19) in (18), thus

$$u(k) = \frac{a_{mr}y_m(k) + b_{mr}r(k) - a^2y(k-1) - abu(k-1)}{b}, \tag{21}$$

and consequently,

$$-\frac{b}{b_{mr}}u(k) - \frac{ab}{b_{mr}}u(k-1) - \frac{a^2}{b_{mr}}y(k-1) + \frac{a_{mr}}{b_{mr}}y_m(k) + r(k) = 0. \tag{22}$$

Arranging the coefficients as adaptive terms, (22) can be written as

$$\theta_1u(k) + \theta_2u(k-1) + \theta_3y(k-1) + \theta_4y_m(k) + r(k) = 0, \tag{23}$$

where the adaptive gains, recalculated for each iteration, are given by $\theta_1 = -\frac{b}{b_{mr}}$, $\theta_2 = -\frac{ab}{b_{mr}}$, $\theta_3 = -\frac{a^2}{b_{mr}}$, and $\theta_4 = \frac{a_{mr}}{b_{mr}}$.

Remark III: Note that the adaptive gains $\boldsymbol{\theta}$ absorb the coefficients of the internal signals, and, consequently, the signals themselves. Since $\boldsymbol{\theta}$ is adapted at each iteration, their signals are also subject to change and can be corrected in case of incorrect initialization, with the exception of θ_1, which should be properly initialized according to Assumption A_I.

Isolating the control action $u(k)$ in (23), it is true that

$$u(k) = \frac{-\theta_2 u(k-1) - \theta_3 y(k-1) - \theta_4 y_m(k) - r(k)}{\theta_1}, \quad (24)$$

being (24) the implementable form in discrete time of the adaptive control action. Furthermore, (23) can be represented in matrix form as

$$\boldsymbol{\theta}^T(k)\boldsymbol{\omega}(k) + r(k) = 0, \quad (25)$$

where $\boldsymbol{\theta}^T(k) = [\ \theta_1(k)\ \ \theta_2(k)\ \ \theta_3(k)\ \ \theta_4(k)\ ]$ and $\boldsymbol{\omega}^T(k) = [\ u(k)\ \ u(k-1)\ \ y(k-1)\ y_m(k)\ ]$.

The AOSAP control gains in $\boldsymbol{\theta}(k)$ will be updated in real time with the adaptation algorithm, as presented next.

3.3 Adaptation algorithm A modified Gradient algorithm is utilized as the parametric adaptation law, allowing real-time adjustment of the controller gains. This approach allows for dynamic tuning of the controller parameters based on the system's evolving conditions. The algorithm is formulated as follows:

$$\boldsymbol{\theta}(k+1) = \boldsymbol{\theta}(k) - \sigma(k)T_s\boldsymbol{\Gamma}\boldsymbol{\theta}(k) - \frac{T_s\kappa\boldsymbol{\Gamma}\boldsymbol{\zeta}(k)\varepsilon(k)}{\bar{m}^2(k)}. \quad (26)$$

As shown in the Lyapunov analysis (Appendix A), the controller maintains boundedness and regulation performance even in the presence of matched and unmatched dynamics, confirming its practical robustness. In this context, $\boldsymbol{\Gamma}$ represents a positive definite square matrix, while κ is a constant designed to accelerate the convergence rate of the controller gains. The term $\bar{m}$ is associated with the majorant and σ refers to the σ-modification function, which will be discussed in detail in subsequent sections. Furthermore, T_s denotes the sampling time and $\boldsymbol{\zeta}$ is the regressor vector, defined as

$$\boldsymbol{\zeta} = W_m(z)\boldsymbol{\omega}. \quad (27)$$

The augmented error, $\varepsilon(k)$, is defined as:

$$\varepsilon(k) = e_1 + \boldsymbol{\theta}^T\boldsymbol{\zeta} + W_m(z)r, \quad (28)$$

being $e_1(k)$ presented and discussed in (10).

For a detailed derivation of the error equation and further insights into the AOSAP theory, the reader is referred to [34]. A bounding signal is introduced, expressed as:

$$\bar{m}^2(k) = m^2(k) + \boldsymbol{\zeta}^T(k)\boldsymbol{\Gamma}\boldsymbol{\zeta}(k), \quad (29)$$

where $m(k)$ evolves according to:

$$m(k+1) = \delta_0 m(k) + \delta_1\big(1 + |u(k)| + |y(k)|\big), \quad (30)$$

with δ_0 and δ_1 as positive design parameters, and the initial condition $m(0) \geq \frac{\delta_1}{1-\delta_0}$. Additionally, the modified gradient algorithm integrates a σ-modification term to avoid parameter divergence, as described in [35]. This modification is defined by:

$$\sigma(k) = \begin{cases} 0 & \text{if } \|\boldsymbol{\theta}(k)\| \leq M_0, \\ \sigma_0\left(\frac{\|\boldsymbol{\theta}(k)\|}{M_0} - 1\right) & \text{if } M_0 < \|\boldsymbol{\theta}(k)\| < 2M_0, \\ \sigma_0 & \text{if } \|\boldsymbol{\theta}(k)\| \geq 2M_0, \end{cases} \quad (31)$$

where σ_0 and M_0 are positive design constants. The term $\sigma(k)$ satisfies $0 \leq \sigma(k) \leq \sigma_0$, with M_0 chosen sufficiently large to account for the unknown true parameter vector $\boldsymbol{\theta}^*$. The majorant ensures that the adaptive system operates within a bounded region by dynamically adjusting $m(k)$, while the σ-modification function is incorporated into the gradient-based adaptation law to introduce a penalization term when the adaptive gain vector $\boldsymbol{\theta}(k)$ exceeds predefined limits [36].

The persistent excitation (PE) condition is fundamental to ensure effective parameter adaptation in MRAC or RMRAC-based controllers. However, these structures are generally not optimal for tracking purely DC references, as a constant reference does not inherently satisfy the PE condition. In this approach, the PE requirement is naturally met due to the characteristics of non-sinusoidal PMSMs. The back-EMF inherently contains harmonic components which, even if minimized, are never entirely eliminated, similar to the chattering behavior in sliding-mode controllers. These harmonics propagate into the stator currents, preventing purely DC conditions and sustaining the necessary excitation. Additionally, practical mismatches, noise, and quantization effects introduce small perturbations that prevent the system from reaching a perfectly steady-state DC response, contributing to PE. Even in stable conditions, variations in load, sensor noise, and disturbances ensure that the adaptation mechanism remains active, allowing the controller to effectively regulate the system.

3.4 Reference Model Design The RMRAC-based controller is implemented in both the d and q coordinates for the current control. Consequently, two reference models need to be chosen, one for each coordinate. The plants are first-order, as discussed above. After considering the system parameters from Table 1 in (4), and discretizing the system with a sampling time of 0.0001 s using the zero-order holder (ZOH) method, it is obtained

$$G_q(z) = G_d(z) = \frac{1.08}{(z - 0.9156)}. \quad (32)$$

It should be noted that the system plant is the same for both the d and q coordinates. Furthermore, the plant follows Assumptions A_I-A_{IV}.

The reference model is tailored to define the desired dynamics of the controlled current signal. To achieve this, it is designed to operate at a frequency an order of magnitude higher than that of the reference signal, ensuring fast and accurate tracking. Furthermore, the model is configured to maintain a gain of 0 dB at the relevant low frequencies, thereby avoiding the introduction of unintended amplification into the reference signal. For the q coordinate, a stable first-order system with a real pole located at $10 \cdot 10^3$ in continuous time was chosen. The discrete-time representation of this reference model is expressed as follows:

$$W_{m(q)}(z) = \frac{0.6321}{(z - 0.3679)}, \quad (33)$$

and for the coordinate d, the stable real pole is located at $1 \cdot 10^3$. The discrete representation of the designed reference model is

$$W_{m(d)}(z) = \frac{0.09516}{(z - 0.9048)}. \quad (34)$$

Both reference models were designed using the ZOH with $T_s = 0.0001$ s, corresponding to $1/f_{sw}$, and furthermore with assumptions A_V and A_{VI}. In addition, the reference model for the q coordinate was designed to be faster than that for the d

coordinate. This choice is justified by the fact that the reference for d is typically 0 A, maintaining a relatively constant dynamic, while the q coordinate tends to exhibit changes in dynamics based on the system's operational conditions. Figure 1 shows the designed reference models $W_{m(q)}(z)$ and $W_{m(d)}(z)$ compared to the plant of the system ($G_q(z) = G_d(z)$).

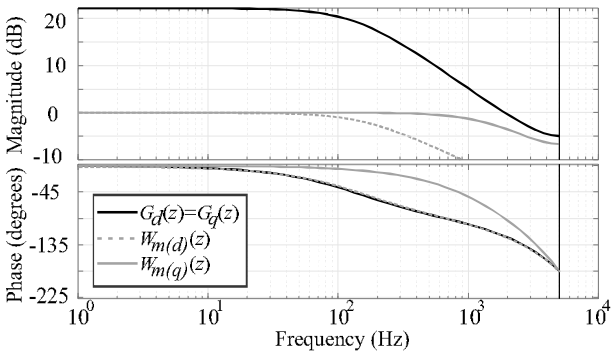

Figure 1: Bode diagram of reference models $W_{m(q)}(z)$ and $W_{m(d)}(z)$ and system plant ($G_q(z) = G_d(z)$).

As presented in Figure 1 and discussed before, the reference models were designed to be faster than the plant dynamics, with $W_{m(q)}(z)$ also faster than $W_{m(d)}(z)$ due to the difference in dynamics between the coordinates. Since the design of the reference models attend to assumptions A_V and A_{VI} and are both stable, they characterize a good choice for the RMRAC-based control structure.

4. Matlab Experiment

After modeling the system plant and presenting the mathematical description of the AOSAP controller, a Matlab simulation of the plant in closed loop was conducted. Including simulation results from Matlab before Hardware-in-the-Loop (HIL) validation serves as an essential intermediate validation step, bridging the gap between theoretical design and real-time implementation. This simulation allows the control algorithm to be evaluated in a purely mathematical environment, free from real-world complications such as transformations, noise, sensing inaccuracies, and modulation effects. It provides a platform for analyzing and fine-tuning the controller's feasibility and performance in handling plant dynamics.

Intermediate simulations are both cost-effective and time-efficient, enabling iterative testing and refinement of the control strategy without hardware-induced complexities. This process significantly reduces the likelihood of encountering unexpected issues during the HIL stage, improving the overall validation workflow, and accelerating the transition to real-time implementation.

For this section, the presented Matlab results focus on the q coordinate control. The plant dynamics in both d and q coordinates is derived from the same underlying physical system and is mathematically equivalent, as shown in (32). Both the d and q coordinate plants are modeled as first-order systems with identical parameters, as determined by the non-sinusoidal PMSM's electrical model. Although minor adjustments in control gains may be required when transitioning between axes, the controller's design and general performance in regulating the q coordinate inherently extend to the d coordinate. By demonstrating the effectiveness of the AOSAP controller in the q coordinate, the results can be generalized to both axes without redundancy.

The experiment involves the adaptive structure controlling the plant presented in (32), using the reference model shown in (33). The control gains Γ and κ were set empirically set to values of 2 and 10, respectively, and the initial values of $\boldsymbol{\theta}$ were $\boldsymbol{\theta}(0)(k) = [\,-2 \;\; -1 \;\; -1 \;\; 1\,]$, randomly initialized. In addition, the following parameters were used: $M_0 = 8$, $\sigma_0 = 0.1$, $\delta_0 = 0.7$, and $\delta_1 = 1$. These values satisfy the limits of the adaptive structure stability analysis, as discussed in [34]. The simulation runs for 200 seconds with a sampling period of $T_s = 0.0001$ seconds. The current reference begins at 10 A. A load step is applied at $t = 66$ seconds, updating r to 20 A. At $t = 100$ seconds, another load step is performed, setting r back to 10 A, which remains constant until the end of the experiment.

Figure 2 shows y_m and y. Figure 2(a) provides an overview, while Figure 2(b) focuses on the first load step. The system output y closely follows the reference model output y_m. After each load step at $t = 66.6$ s and $t = 100$ s, small overshoots of approximately 4% are observed, but the system quickly stabilizes.

Figure 3 illustrates e_1 and ϵ. As expected, the system experiences disturbances at startup and during load steps, temporarily increasing both regulation errors. However, the system rapidly converges to steady state after each disturbance. The tracking (e_1) and augmented (ϵ) errors closely mirror each other throughout the experiment, as ϵ is a function of

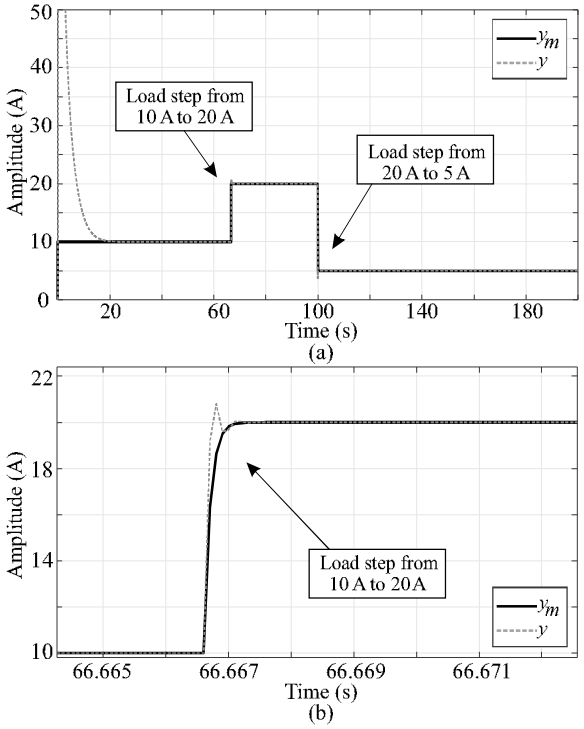

Figure 2: Matlab experiment: reference model y_m and the plant output y.

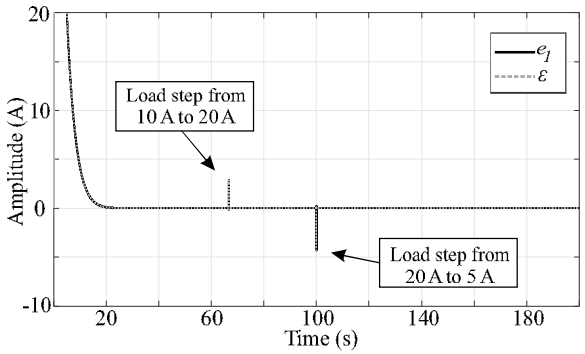

Figure 3: Matlab experiment: tracking error e_1 and the augmented error ϵ.

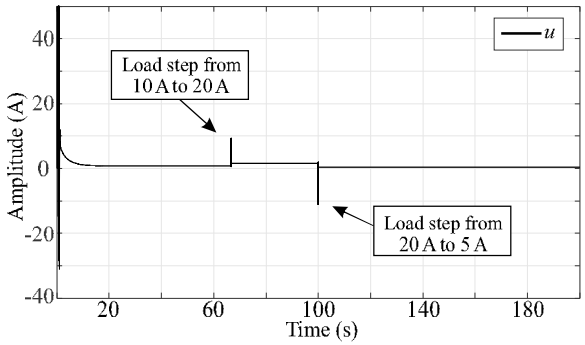

Figure 4: Matlab experiment: control action u.

e_1, as discussed in Section II and equations (10) and (28).

Figure 4 shows the control action u, while Figure 5 shows the auxiliary filter $\boldsymbol{\zeta}$. The control action exhibits a significant transient at startup, but stabilizes once the adaptive parameters minimize the augmented error. The startup transient results from the adaptive controller's initialization with random gains, which requires considerable effort to converge to a suitable $\boldsymbol{\theta}$ close to $\boldsymbol{\theta}^*$. With regard to auxiliary filters, $\boldsymbol{\zeta}$ helps estimate the system dynamics and generate control actions. Stabilization of ζ_1, ζ_2, and ζ_3 near zero after transient indicates stability and rejection disturbance. Furthermore, ζ_4 effectively tracks the reference current r, confirming the controller's ability to achieve desired tracking performance.

Figure 6 shows the adaptive control gains $\boldsymbol{\theta}$. At startup, the adaptive gains exhibit high dynamics due to their initialization far from the actual values. However, the system stabilizes around $t = 20$ s, with adaptive gains showing minimal variations, even in the face of load steps ($t = 66.6$ s and $t = 100$ s). This behavior suggests that the achieved values $\boldsymbol{\theta}$ closely approximate the true gains $\boldsymbol{\theta}^*$, ensuring regulated tracking of y_m by y, even under disturbances.

Simulation-based validation improves the methodological rigor and aligns with industry best practices. It is a standard procedure to ensure reliability and safety before transitioning to physical implementation. The consistency of MATLAB simulation results demonstrates the robustness of the proposed controller, showcasing its effectiveness in regulating plant dynamics in a controlled environment. To mitigate the transient overshoot in the startup, several strategies can be employed. These include selecting a slower reference model,

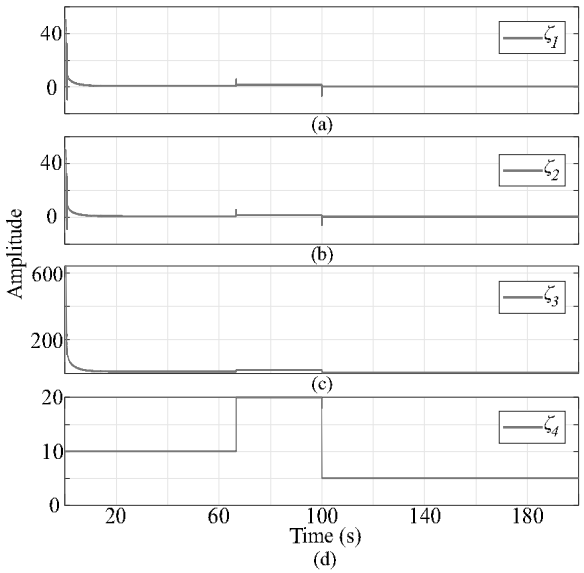

Figure 5: Matlab experiment: auxiliary filters $\boldsymbol{\zeta}$.

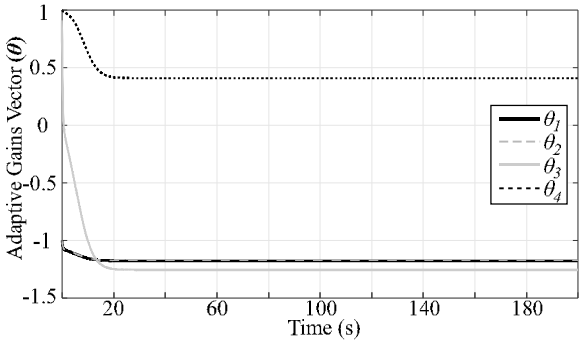

Figure 6: Matlab experiment: adaptive control gains $\boldsymbol{\theta}$.

adjusting the adaptive structure using smaller values of κ, initializing the adaptive gains vector $\boldsymbol{\theta}$ closer to $\boldsymbol{\theta}^*$, or using optimization techniques to determine an optimal set of gains offline, ensuring a more effective initialization. Given the robustness of the adaptive controller to matched and unmatched dynamics, as well as the alignment between the mathematical and physical models, the controller is well suited for implementation in a C-HIL environment. It can be discretized and deployed on a microcontroller or DSP for real-time system control, as will be presented next.

5. Control-Hardware-in-the-Loop Experiment

To facilitate a comprehensive comparison of results achieved with the proposed AOSAP controller, a classical control structure was considered, described later in this section. The setup was established within a C-HIL framework. The system dynamics was emulated using a Typhoon HIL 604 platform, while control strategies were executed on a TMS320F28335 DSP. The system operated with a switching frequency of 10 kHz, which corresponds to a sampling interval of $T_s = 100$ μs. Moreover, full-bridge signals are synthesized considering the space vector modulation presented in [37]. Figure 7 shows the setup of the C-HIL experiment.

The AOSAP structure was tuned using the following de-

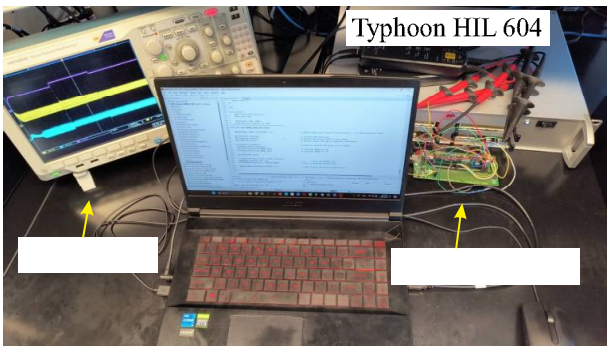

Figure 7: C-HIL experiment setup.

sign parameters for the q coordinate: $\boldsymbol{\Gamma} = 2, \kappa = 10, M_0 = 10$, and $\sigma_0 = 0.1$. Similarly, for the d coordinate, the parameters were set as: $\boldsymbol{\Gamma} = 2, \kappa = 3, M_0 = 5$, and $\sigma_0 = 0.1$. The stability analysis presented in Appendix A and also discussed in [34] indicates a crucial stability condition: $2\|\boldsymbol{\Gamma}\| \cdot |\kappa|^2 T_s^2 \ll 1$. Taking into account his condition with respect to the control gains, the stability of the algorithm is ensured. The initial values of $\boldsymbol{\theta}$ were $\boldsymbol{\theta}(0)(k) = [\ -3 \quad -3 \quad -1 \quad 1\ ]$ for the q coordinate and $\boldsymbol{\theta}(0)(k) = [\ -5 \quad -5 \quad -1 \quad 1\ ]$ for the d coordinate. Both the gains of the controller and the initial values were chosen empirically. On the other hand, the regulation performance of the adaptive structure could be significantly improved by employing a self-tuning methodology [38–40] to optimize the controller dynamics and initial gains. This approach can help reduce transients and obtain better regulation performance without harming stability or robustness.

For comparison with the adaptive controller, a PI was tuned for the coordinates dq. The controller equation for can be described as

$$PI_{(q)}(z) = PI_{(d)}(z) = \frac{0.38593(z - 0.8259)}{(z - 1)}. \qquad (35)$$

The controller of (35) was tuned considering the plant parameters presented in Section II and $T_s = 0.0001$ s. Furthermore, for the non-sinusoidal PMSM velocity control, in the outer loop of the q controller, the following PI was considered (for both experiments), according to [33].

$$PI_{(\omega r)}(z) = \frac{0.673(z - 0.9988)}{(z - 1)}, \qquad (36)$$

also obtained with $T_s = 0.0001$ s. For better understanding, Figure 8 presents the block diagram of the direct adaptive structure for a non-sinusoidal PMSM in dq coordinates.

5.1 Comparison Results For the first experiment, $v_{DC} = 100$ V. The machine initially started with a velocity reference of 40 rad/s and a load of 10 Nm. Throughout this experiment, the velocity reference was adjusted to 50 rad/s and later to 45 rad/s.

Fig. 9 shows a comparison between the proposed AOSAP structure and the classical approach from (35). Channels 1 and 2 of the oscilloscope show the i_q and i_d regulated currents, respectively. Channel 3 shows the regulated machine velocity, w_r. In Fig. 9(a), it is evident that the classical approach can regulate the system but exhibits significant velocity overshoots during transient periods and during velocity steps. In contrast, the proposed system shown in Figure 9(b) shows better performance in regulating the velocity and currents in the dq coordinates, especially for the q coordinate. In particular, both i_q and i_d exhibit reduced current ripple for most of the experiment, leading to lower tracking errors and positively impacting system efficiency. Only after the startup the i_d current exhibited elevated ripple, attributable to the adaptive structure still converging. However, after the velocity steps, both regulated currents demonstrated improved performance. It is important to note that for the regulated velocity (w_r), each measured voltage on the oscilloscope corresponds to 10 rad/s. This is due to the limitations of the Typhoon HIL signal conditioning circuit, where voltage values are restricted within the range of −10 V to 10 V. Values that exceed these limits may harm the HIL device.

Table 2: Torque Ripple comparison.

Load (Nm)	Ripple (Classical)	Ripple (Adaptive)	Improvement
10	15.2782	8.4125	44.94%
12	15.2734	8.4453	44.70%
8	15.4360	8.2391	46.62%

The ripple in regulated currents tends to impact the torque ripple, as discussed in Section II and indicated by (3). Therefore, Figure 10 compares the non-sinusoidal PMSM torque of both controllers. For this experiment, the machine initially operated at 50 rad/s with a load of 10 Nm. This load changed to 12 Nm (at $t = 10$ s) and then to 8 Nm (at $t = 15$ s). As shown in Figure 10, the AOSAP structure significantly reduces torque ripple compared to the PI structure. A detailed comparison of the torque waveforms for both controllers is provided in Table 2. The data in this table demonstrate that the proposed controller achieves substantially lower torque ripple values than the classical structure across all evaluated scenarios, with an average improvement of 45.42%. It is worth noting that the initialization of the vectors $\boldsymbol{\theta}$ and $\boldsymbol{\zeta}$, the reference model choosing, as well as the tuning of the gains Γ and κ, was carried out by an experienced control designer. It is important to highlight that the primary objective of the AOSAP controller is robust adaptive current regulation—not direct torque ripple minimization. Nonetheless, the reduced current and torque ripple observed experimentally is a direct result of improved tracking performance. Moreover, there is significant potential for improvement in performance if these parameters are optimized (especially for startup) using advanced optimization techniques.

6. Experimental Results

After describing the controller and designing and testing it in both MATLAB and the C-HIL setup, this section presents the experimental results that validate the AOSAP control structure in a real-world scenario.

The experimental setup consists of a non-sinusoidal PMSM with the parameters presented in Table 1, driven by a half-bridge inverter, and control algorithms are implemented in a TMS320F28379D DSP from Texas Instruments with a switching and sampling frequency of $f_s = 10kHz$.

Figure 11 presents a picture of the prototype. Importantly, the same control algorithm, reference model, and adaptation gains from the C-HIL setup were retained, with only minor adjustments to the initial values of $\boldsymbol{\theta}(0)$ to accommodate small parameter differences between the hardware-in-

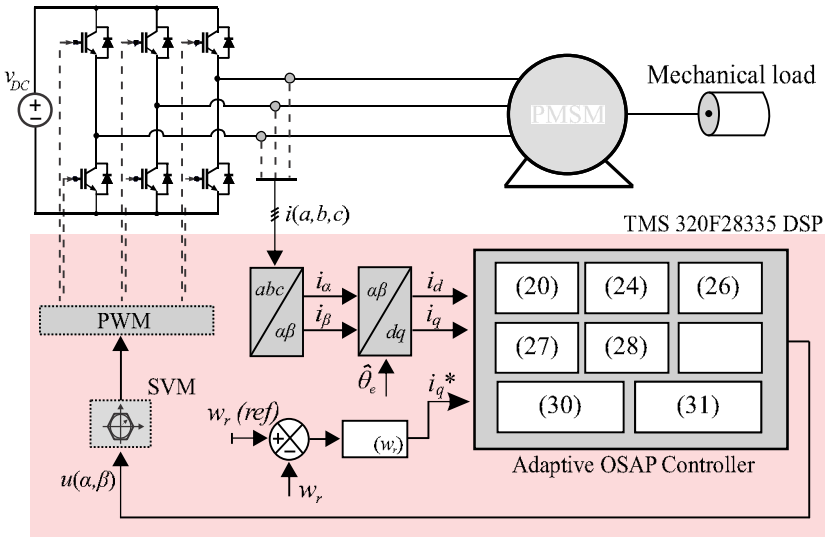

Figure 8: Proposed direct adaptive control structure for non-sinusoidal PMSM in *dq* coordinates.

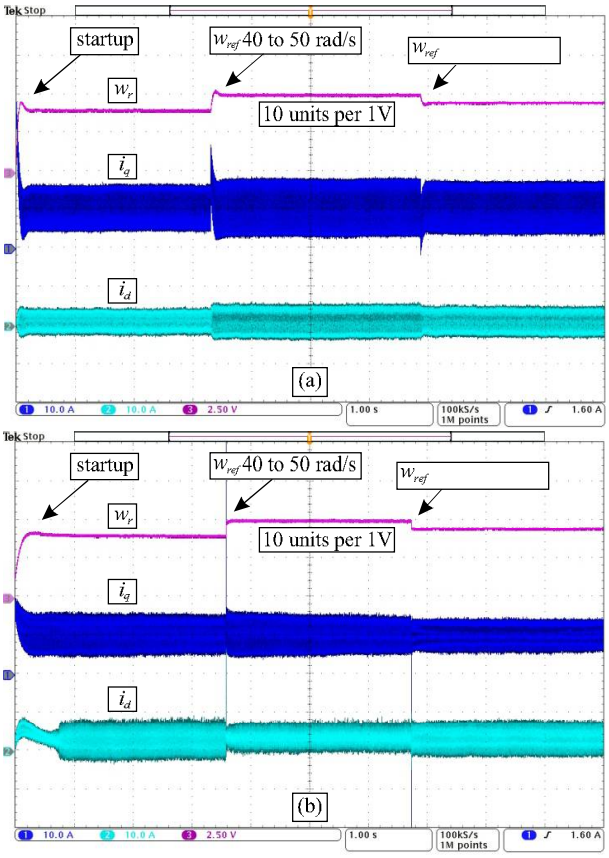

Figure 9: C-HIL: Comparison between the proposed AOSAP and the classical approach. (a) Classical PIs structure (35); (b) AOSAP structure.

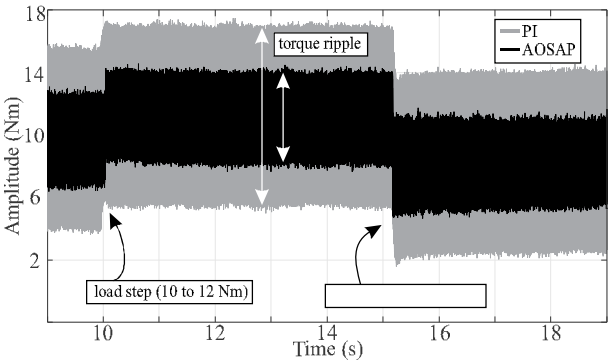

Figure 10: C-HIL: Non-sinusoidal PMSM torque comparison between classical and adaptive structures.

the-loop and the prototype. Specifically, the initial condition was set to $\boldsymbol{\theta}(0)(k)$ = [−2.09918308 1.29651999 −0.00462848414 1.53878868]. This $\boldsymbol{\theta}(0)$ vector was obtained by running the algorithm once with randomly initialized gains and recording the estimated values after convergence, which were then reused as initial conditions for the experiment. This is a common practice in adaptive control applications.

As before, a PI controller was employed for comparison with the proposed structure (designed in the previous section). This baseline is selected not because it represents a performance ceiling, but because it remains the de facto standard in most industrial applications, and demonstrating superiority against it validates the practical relevance of the proposed method.

Fig. 12 presents the velocity results obtained from the prototype. The test scenario lasts 2 seconds, with a reference change occurring at t = 0.45 s. Fig. 12(a) shows ω and ω_r using the proposed adaptive controller throughout the experiment, while Fig. 12(b) and (c) provide zoomed-in views of the intervals $0 < t < 0.4$ s and $1.8 < t < 2$ s, respectively, highlighting the steady-state conditions before and after the velocity step. Similarly, Fig. 12(d) shows the results using the PI controller for the entire experiment, and Fig. 12(e) and (f) detail the same time intervals to observe the steady-state responses. At t = 0.45 s, a significant step change is applied to the velocity reference (from 20 to 30 rad/s). As shown in the figures, both controllers are capable of regulat-

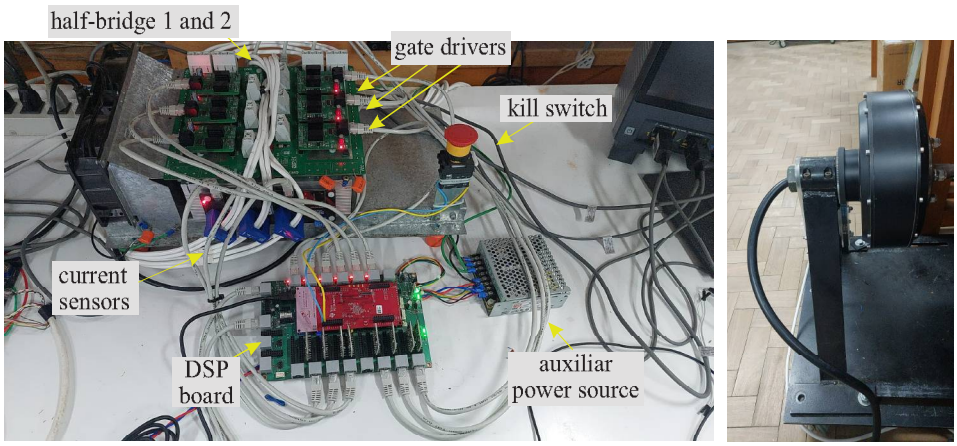

Figure 11: Experimental setup (parameters shown in Table 1). (a) Testbed with the half bridges, gate drivers, auxiliar power source and DSP board; (b) PMSM machine.

ing the system. However, the proposed adaptive controller achieves faster convergence to steady state, reaching 28 rad/s (i.e., 80% of the final value) in 0.12 s, while the PI controller requires 0.796 s to reach the same point—making it 6.6 times slower. In terms of steady-state regulation, the RMS values of the regulated velocity for the adaptive controller were 20.07 rad/s and 30.29 rad/s, compared to 20.10 rad/s and 30.82 rad/s for the PI controller. Therefore, the proposed adaptive structure demonstrated faster transient response and smaller steady-state error than the classical PI controller, confirming the findings from the MATLAB and C-HIL simulations.

Fig. 13 shows the regulated i_q current using the proposed adaptive structure. The current is properly regulated, with the AOSAP control structure exhibiting a noticeable overshoot immediately following the reference step at $t = 0.45$ s. This behavior arises from the one-sample-ahead nature of the controller, which tends to be robust against small errors and unmodeled dynamics but is sensitive to abrupt variations. Nevertheless, this overshoot, combined with the reduced tracking error, results in fast velocity regulation and small steady-state error, as previously discussed and illustrated in Fig. 12. It is also important to highlight that the adaptive structure was tuned empirically. However, its dynamic performance could be further improved by in-depth reference model shaping, initial gain fine tuning, or conducting an offline learning-based optimization to identify a global (or near-global) solution set that more effectively minimizes the tracking error. According to adaptive control theory, multiple parameter sets can satisfy the control objective, but only one optimal set ($\boldsymbol{\theta}^*$) yields the best performance.

Fig. 14 presents the AOSAP control action u. Before the reference step, the average value of the control signal is approximately 11 V. After the reference step, it increases to around 17 V, which is consistent with the velocity update from 20 to 30 rad/s. The same overshoot observed previously is also evident here, with peak values approaching 40 V. Although this overshoot is not desirable, the rapid dynamic response contributes to faster velocity regulation, as discussed earlier. Nonetheless, the overshoot can potentially be mitigated through an offline, optimized tuning process of the controller (to be investigated in a future work).

Fig. 15 shows the majorant m. The purpose of the majorant is to ensure that the internal signals of the controller remain well-behaved, preventing instability. As observed, the majorant values remain stable both before and after the reference step, which aligns with the system's proper steady-state behavior. Additionally, the previously discussed overshoot is reflected here as a sharp peak in the majorant, which acts promptly to prevent the controller from deviating and potentially becoming unstable.

Fig. 16 shows the adaptive gain vector $\boldsymbol{\theta}^*$. It can be observed that the gains remain mostly steady throughout the evaluation period. A slight perturbation, particularly in θ_1, θ_2 and θ_3, is noticeable after the reference step, at $t = 0.45$ s, coinciding with the velocity reference update. This behavior is expected, as the controller adjusts its dynamics to maintain system stability and minimize regulation errors in response to the new operating condition.

The fact that the controller maintained satisfactory performance across different scenarios using the same core structure and tuning validates its inherent adaptability and robustness to model variations. Nonetheless, as discussed previously, the performance of the adaptive structure can be further enhanced through offline self-tuning methodologies such as those proposed in [38, 40], which can optimize initial conditions and adaptation dynamics to reduce transients without compromising stability or general performance.

7. Conclusion

This paper introduced a systematic multilevel validation approach using an adaptive one-sample-ahead preview control structure to regulate a non-sinusoidal PMSM. A comparative analysis with a classical approach demonstrated that the adaptive structure achieved faster regulation and lower tracking errors, resulting in an overall improvement in system efficiency. For future research, learning-based algorithms could be explored to optimize the adaptive controller, along with adaptive harmonic compensation techniques. However, these modifications would require a thorough and different stability analysis of the control structure, since new com-

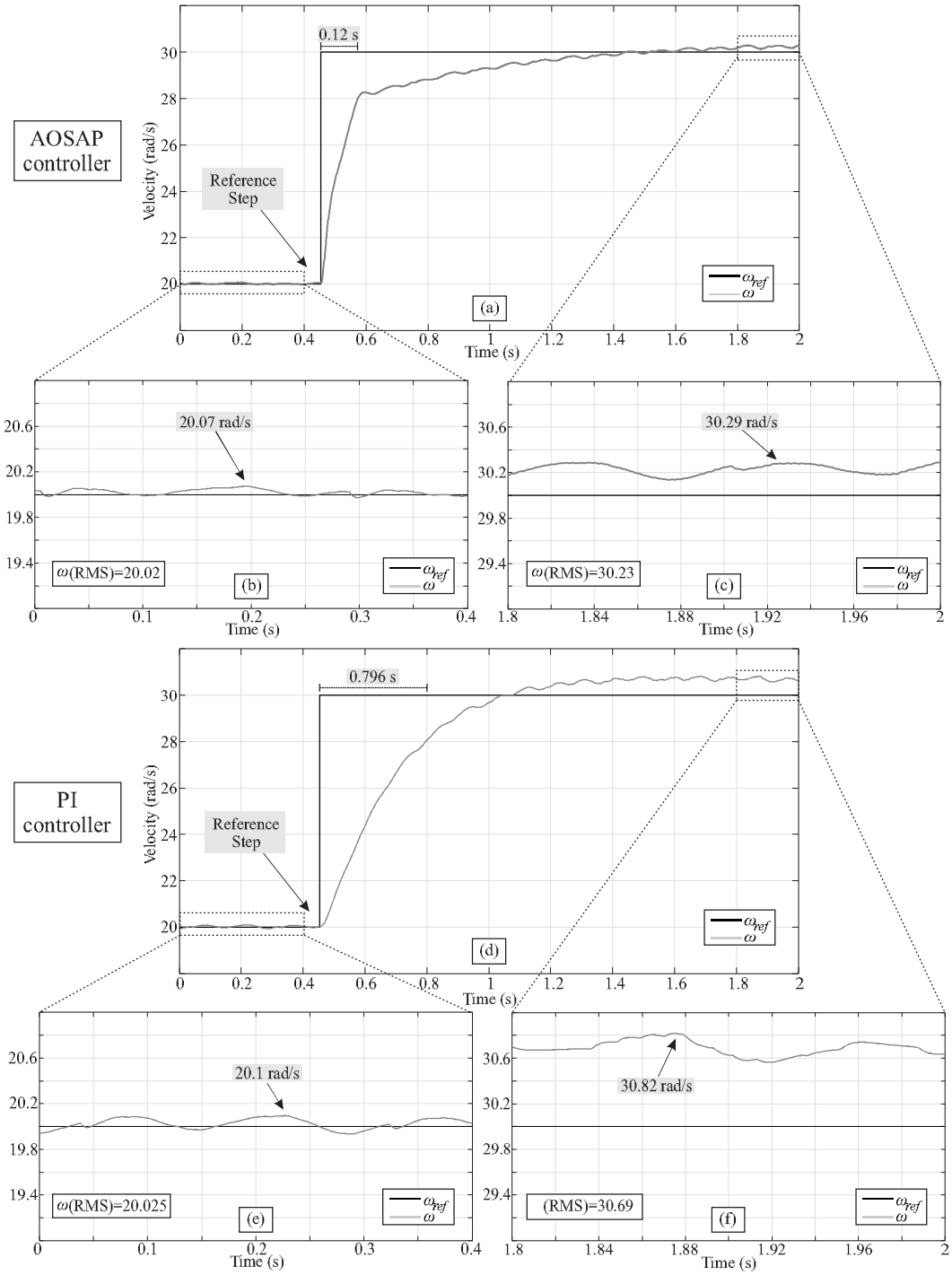

Figure 12: Experimental Result: prototype's regulated velocity. (a),(b),(c) AOSAP ; (d),(e),(f) PI controller for comparison.

ponents would be included in the control algorithm. Furthermore, other adaptive algorithms could be investigated to further improve the control of non-sinusoidal PMSMs, enhance torque harmonic compensation, and boost overall performance while keeping robustness to matched and unmatched dynamics.

Appendix: Stability Analysis

Theorem 1: *Considering the presented adaptive control law, whose adaptation algorithm is described by* (26)*, with the system plant* $G(z)$ *defined in* (7)*, subject to assumptions* A_I *to* A_{IV} *and the reference model* $W_m(z)$*, given by* (12)*, is subject to assumptions* A_V*-*A_{VI}*. The closed-loop system is robust, and it is possible that the tracking error* $e_1(k) \to 0$ *when* $k \to \infty$ *or, at least,* $e_1(k)$ *is small on average and belongs to a residual set.*

Proof: Consider the following discrete-time Lyapunov candidate:

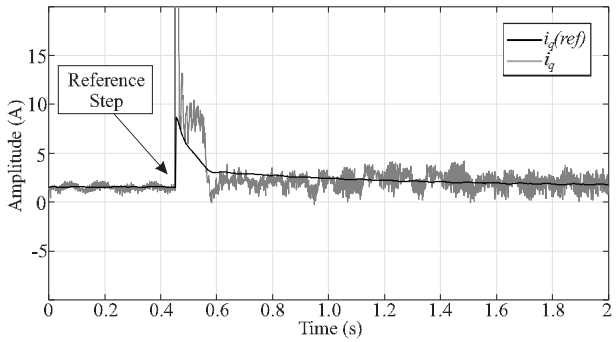

Figure 13: Experimental result: AOSAP regulated current.

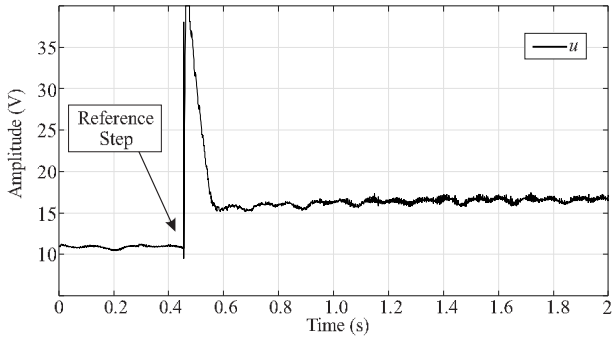

Figure 14: Experimental result: AOSAP control action.

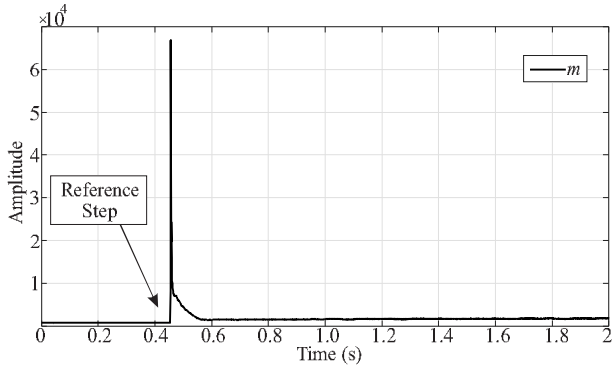

Figure 15: Experimental result: AOSAP majorant signal.

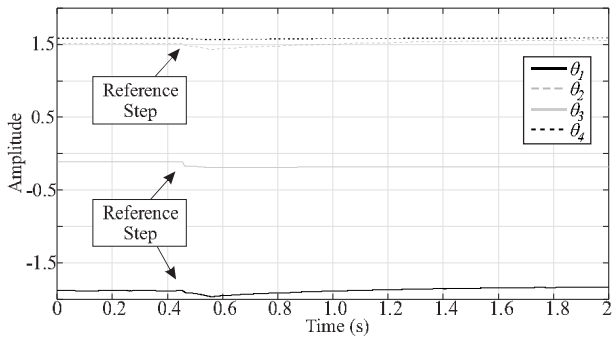

Figure 16: Experimental result: $\boldsymbol{\theta}$ gains obtained in the experimental test.

$$V(k) = \boldsymbol{\phi}(k)^T \boldsymbol{\Gamma}^{-1} \boldsymbol{\phi}(k). \tag{37}$$

The finite variation of the Lyapunov candidate is

$$\Delta V(k) = \boldsymbol{\phi}(k+1)^T \boldsymbol{\Gamma}^{-1} \boldsymbol{\phi}(k+1) - \boldsymbol{\phi}(k)^T \boldsymbol{\Gamma}^{-1} \boldsymbol{\phi}(k). \tag{38}$$

As $\Delta\boldsymbol{\phi}(k) = \boldsymbol{\phi}(k+1) - \boldsymbol{\phi}(k)$,

$$\begin{aligned}\boldsymbol{\phi}(k)^T \boldsymbol{\Gamma}^{-1} \boldsymbol{\phi}(k) = \boldsymbol{\phi}(k+1)^T \boldsymbol{\Gamma}^{-1} \boldsymbol{\phi}(k+1) - \boldsymbol{\phi}(k+1)^T \boldsymbol{\Gamma}^{-1} \Delta\boldsymbol{\phi}(k) - \\ \Delta\boldsymbol{\phi}(k)^T \boldsymbol{\Gamma}^{-1} \boldsymbol{\phi}(k+1) + \Delta\boldsymbol{\phi}(k)^T \boldsymbol{\Gamma}^{-1} \Delta\boldsymbol{\phi}(k).\end{aligned} \tag{39}$$

From (39), follows

$$\begin{aligned}\boldsymbol{\phi}(k)^T \boldsymbol{\Gamma}^{-1} \boldsymbol{\phi}(k) = \boldsymbol{\phi}(k+1)^T \boldsymbol{\Gamma}^{-1} \boldsymbol{\phi}(k+1) - \\ 2\boldsymbol{\phi}(k+1)^T \boldsymbol{\Gamma}^{-1} \Delta\boldsymbol{\phi}(k) + \Delta\boldsymbol{\phi}(k)^T \boldsymbol{\Gamma}^{-1} \Delta\boldsymbol{\phi}(k),\end{aligned} \tag{40}$$

and replacing (40) on (38), it is obtained

$$\begin{aligned}\Delta V(k) = 2\boldsymbol{\phi}(k+1)^T \boldsymbol{\Gamma}^{-1} \Delta\boldsymbol{\phi}(k) - \\ \Delta\boldsymbol{\phi}(k)^T \boldsymbol{\Gamma}^{-1} \Delta\boldsymbol{\phi}(k) \leq 2\boldsymbol{\phi}(k+1)^T \boldsymbol{\Gamma}^{-1} \Delta\boldsymbol{\phi}(k).\end{aligned} \tag{41}$$

Next, it is subtracted $\boldsymbol{\theta}^*$ on both sides of (26), resulting in

$$\boldsymbol{\phi}(k+1) = \boldsymbol{\phi}(k) - \sigma(k) T_S \boldsymbol{\Gamma} \boldsymbol{\theta}(k) - \frac{T_S \kappa \boldsymbol{\Gamma} \boldsymbol{\xi}(k) \varepsilon(k)}{\bar{m}(k)^2}. \tag{42}$$

Note that $\boldsymbol{\zeta}$ was replaced by $\boldsymbol{\xi}$, but they are equivalent. This is done only for formal proof purposes. Replacing (42) into (41), it is obtained

$$\begin{aligned}\Delta V(k) \leq 2\left(\boldsymbol{\phi}(k) - \sigma(k) T_S \boldsymbol{\Gamma} \boldsymbol{\theta}(k) - \frac{T_S \kappa \boldsymbol{\Gamma} \boldsymbol{\xi}(k) \varepsilon(k)}{\bar{m}(k)^2}\right)^T \\ \boldsymbol{\Gamma}^{-1} \left(-\sigma(k) T_S \boldsymbol{\Gamma} \boldsymbol{\theta}(k) - \frac{T_S \kappa \boldsymbol{\Gamma} \boldsymbol{\xi}(k) \varepsilon(k)}{\bar{m}(k)^2}\right),\end{aligned} \tag{43}$$

and then,

$$\begin{aligned}\Delta V(k) \leq -2\sigma(k) T_S \boldsymbol{\phi}(k)^T \boldsymbol{\theta}(k) + 2\sigma_k^2 {T_S}^2 \boldsymbol{\theta}_k^T \boldsymbol{\Gamma} \boldsymbol{\theta}(k) + \\ \frac{2\sigma(k) {T_S}^2 \kappa \boldsymbol{\xi}(k)^T \boldsymbol{\Gamma} \boldsymbol{\theta}_k \varepsilon(k)}{\bar{m}(k)^2} - \frac{2 T_S \kappa \boldsymbol{\phi}(k)^T \boldsymbol{\xi}(k) \varepsilon(k)}{\bar{m}(k)^2} + \\ \frac{2\sigma(k) {T_S}^2 \kappa \boldsymbol{\theta}(k)^T \boldsymbol{\Gamma} \boldsymbol{\xi}(k) \varepsilon(k)}{\bar{m}(k)^2} + \frac{2 {T_S}^2 \kappa^2 \boldsymbol{\Gamma} \boldsymbol{\xi}(k)^T \boldsymbol{\xi}(k) \varepsilon_k^2}{\bar{m}(k)^2 \bar{m}(k)^2}.\end{aligned} \tag{44}$$

Besides, from (44), it also follows

$$\begin{aligned}\Delta V(k) \leq -2\sigma(k) T_S \boldsymbol{\phi}(k)^T \boldsymbol{\theta}(k) + \\ 2\sigma(k)^2 {T_S}^2 \boldsymbol{\theta}(k)^T \boldsymbol{\Gamma} \boldsymbol{\theta}(k) - \frac{2 T_S \kappa \boldsymbol{\phi}(k)^T \boldsymbol{\xi}(k) \varepsilon(k)}{\bar{m}(k)^2} + \\ \frac{4\sigma(k) {T_S}^2 \kappa \boldsymbol{\theta}(k)^T \boldsymbol{\Gamma} \boldsymbol{\xi}(k) \varepsilon(k)}{\bar{m}(k)^2} + \frac{2 {T_S}^2 \kappa^2 \boldsymbol{\Gamma} \boldsymbol{\xi}(k)^T \boldsymbol{\xi}(k) \varepsilon^2(k)}{\bar{m}^2(k) \bar{m}^2(k)}.\end{aligned} \tag{45}$$

The augmented error presented in (28) can be rewritten as

$$\varepsilon(k) = \bar{\boldsymbol{\phi}}(k)^T \boldsymbol{\xi}(k) + \mu\eta(k), \tag{46}$$

and for implementation purposes, it is considered as

$$\varepsilon = e_1 + \bar{\boldsymbol{\theta}}^T \boldsymbol{\xi} + W_m(z) r, \tag{47}$$

as discussed in Section 2. More information about this augmented error mathematical development can be found in [34].

Replacing (46) into (45), results in

$$\Delta V(k) \leq -2T_S\sigma(k)\boldsymbol{\phi}(k)^T\boldsymbol{\theta}(k) + 2\sigma(k)^2{T_S}^2\boldsymbol{\theta}(k)^T\boldsymbol{\Gamma}\boldsymbol{\theta}(k) - \frac{2T_S\kappa\left(\boldsymbol{\phi}(k)^T\boldsymbol{\xi}(k)\right)^2}{\bar{m}(k)^2} - \frac{2T_S\kappa\boldsymbol{\phi}(k)^T\boldsymbol{\xi}(k)\mu\eta(k)}{\bar{m}(k)^2} + \frac{4\sigma(k){T_S}^2\kappa\boldsymbol{\theta}(k)^T\boldsymbol{\Gamma}\boldsymbol{\xi}(k)\varepsilon(k)}{\bar{m}(k)^2} + \frac{2{T_S}^2\kappa^2\boldsymbol{\Gamma}\boldsymbol{\xi}(k)^T\boldsymbol{\xi}(k)\varepsilon(k)^2}{\bar{m}(k)^2\bar{m}(k)^2}, \tag{48}$$

which is equivalent to

$$\Delta V(k) \leq -2T_S\sigma(k)\boldsymbol{\phi}(k)^T\boldsymbol{\theta}(k) + 2\sigma(k)^2{T_S}^2\boldsymbol{\theta}(k)^T\boldsymbol{\Gamma}\boldsymbol{\theta}(k) - \frac{T_S\kappa(\boldsymbol{\phi}(k)^T\boldsymbol{\xi}(k))^2}{\bar{m}(k)^2} - \frac{T_S\kappa(\boldsymbol{\phi}(k)^T\boldsymbol{\xi}(k))^2}{\bar{m}(k)^2} - \frac{2T_S\kappa\boldsymbol{\phi}(k)^T\boldsymbol{\xi}(k)\mu\eta(k)}{\bar{m}(k)^2} + \frac{4\sigma(k){T_S}^2\kappa\boldsymbol{\theta}(k)^T\boldsymbol{\Gamma}\boldsymbol{\xi}(k)\varepsilon(k)}{\bar{m}(k)^2} + \frac{2{T_S}^2\kappa^2\boldsymbol{\Gamma}\boldsymbol{\xi}(k)^T\boldsymbol{\xi}(k)\varepsilon(k)^2}{\bar{m}(k)^2\bar{m}(k)^2}. \tag{49}$$

Equation (49) can also be written as

$$\Delta V(k) \leq -2T_S\sigma(k)\boldsymbol{\phi}(k)^T\boldsymbol{\theta}(k) + 2\sigma(k)^2{T_S}^2\boldsymbol{\theta}(k)^T\boldsymbol{\Gamma}\boldsymbol{\theta}(k) - \frac{T_S\kappa(\boldsymbol{\phi}(k)^T\boldsymbol{\xi}(k))^2}{\bar{m}(k)^2} - \frac{T_S\kappa(\boldsymbol{\phi}(k)^T\boldsymbol{\xi}(k)+\mu\eta(k))^2}{\bar{m}(k)^2} + \frac{T_S\kappa(\mu\eta(k))^2}{\bar{m}(k)^2} + \frac{4\sigma(k){T_S}^2\kappa\boldsymbol{\theta}(k)^T\boldsymbol{\Gamma}\boldsymbol{\xi}(k)\varepsilon(k)}{\bar{m}(k)^2} + \frac{2{T_S}^2\kappa^2\boldsymbol{\Gamma}\boldsymbol{\xi}(k)^T\boldsymbol{\xi}(k)\varepsilon(k)^2}{\bar{m}(k)^2\bar{m}(k)^2}. \tag{50}$$

Furthermore, as

$$2\sigma(k)^2{T_S}^2\boldsymbol{\theta}(k)^T\boldsymbol{\Gamma}\boldsymbol{\theta}(k) + \frac{4\sigma(k){T_S}^2\kappa\boldsymbol{\theta}(k)^T\boldsymbol{\Gamma}\boldsymbol{\xi}(k)\varepsilon(k)}{\bar{m}(k)^2} + \frac{2{T_S}^2\kappa^2\boldsymbol{\Gamma}\boldsymbol{\xi}(k)^T\boldsymbol{\xi}(k)\varepsilon(k)^2}{\bar{m}(k)^2\bar{m}(k)^2} = 2{T_S}^2\left(\sigma(k)\boldsymbol{\theta}(k) + \frac{\kappa\boldsymbol{\xi}(k)\varepsilon(k)}{\bar{m}(k)^2}\right)^T\boldsymbol{\Gamma}\left(\sigma(k)\boldsymbol{\theta}(k) + \frac{\kappa\boldsymbol{\xi}(k)\varepsilon(k)}{\bar{m}(k)^2}\right), \tag{51}$$

therefore, (50) can be expressed as

$$\Delta V(k) \leq -2T_S\sigma(k)\boldsymbol{\phi}(k)^T\boldsymbol{\theta}(k) - \frac{T_S\kappa(\boldsymbol{\phi}(k)^T\boldsymbol{\xi}(k))^2}{\bar{m}(k)^2} - \frac{T_S\kappa(\boldsymbol{\phi}(k)^T\boldsymbol{\xi}(k)+\mu\eta(k))^2}{\bar{m}(k)^2} + \frac{T_S\kappa(\mu\eta(k))^2}{\bar{m}(k)^2} + 2{T_S}^2\|\boldsymbol{\Gamma}\|\left\|\sigma(k)\boldsymbol{\theta}(k) + \frac{\kappa\boldsymbol{\xi}(k)\varepsilon(k)}{\bar{m}(k)^2}\right\|^2, \tag{52}$$

which is equivalent to

$$\Delta V(k) \leq -2T_S\sigma(k)\boldsymbol{\phi}(k)^T\boldsymbol{\theta}(k) - \frac{T_S\kappa(\boldsymbol{\phi}(k)^T\boldsymbol{\xi}(k))^2}{\bar{m}(k)^2} - \frac{T_S\kappa(\boldsymbol{\phi}(k)^T\boldsymbol{\xi}(k)+\mu\eta(k))^2}{\bar{m}(k)^2} + \frac{T_S\kappa(\mu\eta(k))^2}{\bar{m}(k)^2} + 2{T_S}^2\|\boldsymbol{\Gamma}\|\left(\|\sigma(k)\boldsymbol{\theta}(k)\|^2 + \left\|\frac{\kappa\boldsymbol{\xi}(k)\varepsilon(k)}{\bar{m}(k)^2}\right\|^2\right). \tag{53}$$

In addition, (53) can be rearranged to be expressed as

$$\Delta V(k) \leq -2T_S\sigma(k)\boldsymbol{\phi}(k)^T\boldsymbol{\theta}(k) - \frac{T_S\kappa(\boldsymbol{\phi}(k)^T\boldsymbol{\xi}(k))^2}{\bar{m}(k)^2} - \frac{T_S\kappa\varepsilon(k)^2}{\bar{m}(k)^2} + \frac{T_S\kappa(\mu\eta(k))^2}{\bar{m}(k)^2} + 2{T_S}^2\sigma(k)^2\|\boldsymbol{\Gamma}\|.\|\boldsymbol{\theta}(k)\|^2 + 2{T_S}^2\|\boldsymbol{\Gamma}\|.|\kappa|^2\left\|\frac{\boldsymbol{\xi}(k)}{\bar{m}(k)}\right\|^2\left\|\frac{\varepsilon(k)}{\bar{m}(k)}\right\|^2. \tag{54}$$

From it, the following inequality is obtained

$$\Delta V(k) \leq -2T_S\sigma(k)\boldsymbol{\phi}(k)^T\boldsymbol{\theta}(k) - T_S\kappa\frac{\varepsilon(k)^2}{\bar{m}(k)^2}\left(1 - 2{T_S}^2\|\boldsymbol{\Gamma}\|.|\kappa|^2\frac{\|\boldsymbol{\xi}(k)\|^2}{\bar{m}(k)^2}\right) - \frac{T_S\kappa(\boldsymbol{\phi}(k)^T\boldsymbol{\xi}(k))^2}{\bar{m}(k)^2} + \frac{T_S\kappa(\mu\eta(k))^2}{\bar{m}(k)^2} + 2{T_S}^2\sigma(k)^2\|\boldsymbol{\Gamma}\|\|\boldsymbol{\theta}(k)\|^2. \tag{55}$$

As $(\phi-\theta)^T(\phi-\theta) = \|\theta^*\|^2 = \|\phi\|^2 - 2\phi^T\theta + \|\theta\|^2$, therefore $-2\phi^T\theta \leq \|\theta^*\|^2 - \|\theta\|^2$. Thereby, it can be stated that

$$-2T_S\sigma(k)\boldsymbol{\phi}(k)^T\boldsymbol{\theta}(k) \leq T_S\sigma(k)\|\theta^*\|^2 - T_S\sigma(k)\|\boldsymbol{\theta}(k)\|^2. \tag{56}$$

Next, replacing (56) into (55), it is obtained

$$\Delta V(k) \leq -T_S\sigma(k)\|\boldsymbol{\theta}(k)\|^2 + T_S\sigma(k)\|\theta^*\|^2 + 2{T_S}^2\sigma(k)^2\|\boldsymbol{\Gamma}+\|\|\boldsymbol{\theta}(k)\|^2 - T_S\kappa\frac{\varepsilon(k)^2}{\bar{m}(k)^2}\left(1 - 2{T_S}^2\|\boldsymbol{\Gamma}\|.|\kappa|^2\frac{\|\boldsymbol{\xi}(k)\|^2}{\bar{m}(k)^2}\right) - \frac{T_S\kappa(\boldsymbol{\phi}(k)^T\boldsymbol{\xi}(k))^2}{\bar{m}(k)^2} + \frac{T_S\kappa(\mu\eta(k))^2}{\bar{m}(k)^2}, \tag{57}$$

and from previous equation, it can be concluded that

I) Once $\frac{\|\boldsymbol{\xi}(k)\|^2}{\bar{m}(k)^2} < 1$, because $\bar{m}(k)^2 > \|\boldsymbol{\xi}(k)\|^2$, then

$$2{T_S}^2\|\boldsymbol{\Gamma}\|.|\kappa|^2\frac{\|\boldsymbol{\xi}(k)\|^2}{\bar{m}(k)^2} << 1, \tag{58}$$

can be valid, because T_s, κ, and $\boldsymbol{\Gamma}$ are designer defined. Therefore, $\left(1 - 2{T_S}^2\|\boldsymbol{\Gamma}\|.|\kappa|^2\frac{\|\boldsymbol{\xi}(k)\|^2}{\bar{m}(k)^2}\right)$ is a positive value and $-T_S\kappa\frac{\varepsilon(k)^2}{\bar{m}(k)^2}\left(1 - 2{T_S}^2\|\boldsymbol{\Gamma}\|.|\kappa|^2\frac{\|\boldsymbol{\xi}(k)\|^2}{\bar{m}_k^2}\right) < 0$.

The demonstration of the boundedness of the closed-loop signals by a majorant signal, $m(k)$, is based in the work of Ioannou and Tsakalis [41]. Therefore, it is here omitted; however, it is presented in detail in [34].

II) As mentioned earlier, T_S, $\boldsymbol{\Gamma}$ and κ are positive constants defined by designer. Therefore, they can be chosen such that $-\frac{T_s\kappa\left(\boldsymbol{\phi}^T(k)\boldsymbol{\xi}(k)\right)^2}{\bar{m}^2(k)}$ is negative.

From (31) and (57), it can be verified that $-T_S\sigma(k)\|\boldsymbol{\theta}(k)\|^2 + T_S\sigma(k)\|\boldsymbol{\theta}^*\|^2 + 2{T_S}^2\sigma(k)^2\|\boldsymbol{\Gamma}\|\|\boldsymbol{\theta}(k)\|^2 \leq 0$, or yet

$$T_S\sigma(k)\left(-\|\boldsymbol{\theta}(k)\|^2+\|\boldsymbol{\theta}^*\|^2+2T_S\sigma(k)\,\|\boldsymbol{\Gamma}\|\,\|\boldsymbol{\theta}(k)\|^2\right)\leq 0. \tag{59}$$

Besides, considering $\|\boldsymbol{\theta}(k)\| \geq 2M_0$ in (59), and using (31), it is possible to find out values for T_S, $\boldsymbol{\Gamma}$ and $\sigma(k)$ such that $8T_S\sigma(k)\,\|\boldsymbol{\Gamma}\|\,{M_0}^2 << 1$ is satisfied. Moreover, $0 \leq \|\boldsymbol{\theta}(k)\| \leq M_0 \Rightarrow \sigma(k) = 0$ and therefore (59) is null. In addition, on interval $M_0 < \|\boldsymbol{\theta}(k)\| < 2M_0$, $\sigma(k) \to 0$ as $\|\boldsymbol{\theta}(k)\| \to M_0$ and (59) still being negative and will tend to zero when $\|\boldsymbol{\theta}(k)\| \to M_0$. Besides, it is affirmed that $\|\boldsymbol{\theta}^*\| \leq \beta M_0$ with $0 < \beta < 1$. Then, from (57),

$$\Delta V(k) \leq \frac{T_S\,\kappa(\mu\eta(k))^2}{\bar{m}(k)^2}. \tag{60}$$

Finally, from (57)-(60), it can be concluded that $\Delta V(k)$ is almost always negative, and as $\Delta V(k) < 0$, all elements which compound the Lyapunov candidate function are limited. Eventually, $\Delta V(k) > 0$ and consequently $\boldsymbol{\phi}(k)$ and $\boldsymbol{\theta}(k)$ tend to increase until (57) return naturally to a negative value. Therefore, it can be affirmed that $V(k)$ is upperly limited by $V_0(k)$ as follows,

$$V_0(k) = \frac{T_S\,\kappa(\mu\eta(k))^2}{\bar{m}(k)^2}. \tag{61}$$

In other words, if the algorithm fails to find a suitable solution set that achieves zero tracking error, there will be a residual error due to unmodeled dynamics. However, it is important to note that the tracking error will be small on average and remain bounded above, as indicated by (57)-(61). ■

Acknowledgments

The authors would like to express their sincere gratitude to the editor and reviewers for their invaluable feedback and insightful comments, which greatly improved the quality of this work. The work of Guilherme Vieira Hollweg, Van-Hai Bui, Mengqi Wang, and Wencong Su was supported in part by the U.S. National Science Foundation under Grant 2321661. Any opinions, findings, conclusions, or recommendations expressed in this material are those of the authors and do not necessarily reflect the views of the National Science Foundation. The authors also would like to thank Typhoon HIL© for the research support.

References

(1) G. V. Hollweg, L. R. Rocha, B. Van-Hai, R. P. Vieira, M. Wang, and W. Su, "Adaptive one sample ahead preview control for nonsinusoidal pmsm with *dq* coordinate implementation," in *27th International Conference on Electrical Machines and Systems (ICEMS2024-Fukuoka), Fukuoka, Japan, November 2024*.

(2) G. Harper, R. Sommerville, E. Kendrick, L. Driscoll, P. Slater, R. Stolkin, A. Walton, P. Christensen, O. Heidrich, S. Lambert *et al.*, "Recycling lithium-ion batteries from electric vehicles," *Nature*, vol. 575, no. 7781, pp. 75–86, 2019.

(3) J. A. Sanguesa, V. Torres-Sanz, P. Garrido, F. J. Martinez, and J. M. Marquez-Barja, "A review on electric vehicles: Technologies and challenges," *Smart Cities*, vol. 4, no. 1, pp. 372–404, 2021.

(4) IEA, "World energy outlook 2022." IEA Paris, France, 2022.

(5) D. Kumar, R. K. Nema, and S. Gupta, "A comparative review on power conversion topologies and energy storage system for electric vehicles," *Int. Journal of Energy Research*, vol. 44, no. 10, pp. 7863–7885, 2020.

(6) G. V. Hollweg, P. J. D. de Oliveira Evald, R. V. Tambara, and H. A. Gründling, "A robust adaptive super-twisting sliding mode controller applied on grid-tied power converter with an LCL filter," *Control Engineering Practice*, vol. 122, p. 105104, 2022.

(7) Y. Zuo, C. Lai, and K. L. V. Iyer, "A review of sliding mode observer based sensorless control methods for PMSM drive," *IEEE Transactions on Power Electronics*, 2023.

(8) J. Yan, Y. Feng, and J. Dong, "Study on dynamic characteristic of wind turbine emulator based on PMSM," *Renewable Energy*, vol. 97, pp. 731–736, 2016.

(9) R. Sreejith and B. Singh, "Sensorless predictive current control of PMSM EV drive using dsogi-fll based sliding mode observer," *IEEE Trans. on Industrial Electronics*, vol. 68, no. 7, pp. 5537–5547, 2020.

(10) D. Hiroe, X. Zhang, K. Nakamura, K. Sato, R. Suzuki, K. Yoshimoto, and T. Yokoyama, "A study of 10mhz multi-sampling deadbeat control for pmsm drive system using uspm controller," *IEEJ Journal of Industry Applications*, vol. 12, no. 3, pp. 508–516, 2023.

(11) Y. Ito and Y. Iwaji, "Harmonic reduction method using minor sampling process for sensorless signal injection-based position control technique," *IEEJ Journal of Industry Applications*, vol. 12, no. 4, pp. 719–725, 2023.

(12) H.-W. Lee, J.-H. Hwang, and K.-B. Lee, "Simplified deadbeat predictive torque control based on discrete space vector modulation for driving an open-end winding permanent magnet synchronous motor," *IEEJ Journal of Industry Applications*, vol. 13, no. 3, pp. 308–316, 2024.

(13) R. Krishnan, *Permanent magnet synchronous and brushless DC motor drives*. CRC press, 2017.

(14) X. Xiao and C. Chen, "Reduction of torque ripple due to demagnetization in PMSM using current compensation," *IEEE transactions on applied superconductivity*, vol. 20, no. 3, pp. 1068–1071, 2010.

(15) J. F. Gieras, R.-J. Wang, and M. J. Kamper, *Axial flux permanent magnet brushless machines*. Springer Science & Business Media, 2008.

(16) A. G. de Castro, W. C. A. Pereira, T. E. P. de Almeida, C. M. R. de Oliveira, J. R. B. de Almeida Monteiro, and A. A. de Oliveira, "Improved finite control-set model-based direct power control of BLDC motor with reduced torque ripple," *IEEE Transactions on Industry Applications*, vol. 54, no. 5, pp. 4476–4484, 2018.

(17) Z. Lyu, L. Wu, J. Yi, and S. Yang, "Hybrid frame-based current control scheme for lc-equipped pmsm with non-sinusoidal back-emf," *IEEE Transactions on Power Electronics*, vol. 38, no. 5, pp. 5994–6004, 2023.

(18) A. Abbaszadeh, D. Arab Khaburi, and J. Rodríguez, "Predictive control of permanent magnet synchronous motor with non-sinusoidal flux distribution for torque ripple minimisation using the recursive least square identification method," *IET Electric Power Applications*, vol. 11, no. 5, pp. 847–856, 2017.

(19) L. Guo, G. Zhou, N. Song, M. Zhu, and Y. Mu, "An enhanced parallel-observer based deadbeat predictive control method for PMSM with non-sinusoidal back-emf," *IEEE Access*, 2023.

(20) Z. Sun, C. Tan, B. Li, A. Song, P. Yu, and M. Hao, "Dual model predictive control strategy of direct-drive pmsm based on sliding mode disturbance observer," *IEEJ Transactions on Electrical and Electronic Engineering*, vol. 19, no. 4, pp. 527–534, 2024.

(21) H. Nian, C. Wu, and P. Cheng, "Direct resonant control strategy for torque ripple mitigation of DFIG connected to DC link through diode rectifier on stator," *IEEE Transactions on Power Electronics*, vol. 32, no. 9, pp. 6936–6945, 2016.

(22) O. M. E. Mohammed, W. Xu, Y. Liu, and F. Blaabjerg, "An improved control method for standalone brushless doubly fed induction generator under unbalanced and nonlinear loads using dual-resonant controller," *IEEE Trans. on Ind. Electronics*, vol. 68, no. 7, pp. 5594–5605, 2020.

(23) K. Guo, M. Yang, X. Li, P. Shi, and P. Wang, "Research on a new adaptive integral sliding mode controller based on a small BLDC," *IEEE Access*, vol. 10, pp. 73 204–73 213, 2022.

(24) M. Shirvani Boroujeni, G. Arab Markadeh, J. Soltani, and F. Blaabjerg, "Torque ripple reduction of brushless DC motor with harmonic current injection based on integral terminal sliding mode control," *IET Electric Power Applications*, vol. 12, no. 1, pp. 25–36, 2018.

(25) Q. Zhang, Y. Fan, J. Chen, C. Yang, and M. Cheng, "A current harmonic suppression method for PMSM based on harmonic prediction adaptive notch filter," *IEEE Transactions on Energy Conversion*, vol. 37, no. 3, pp. 2107–2118, 2022.

(26) Z. Lyu, S. Niu, T. Wang, L. Wu, and K. Chau, "Virtual multiphase drive-based harmonic current injection approach for pmsms with distorted back-emfs," *IEEE Transactions on Power Electronics*, 2024.

(27) A. G. de Castro, P. R. U. Guazzelli, C. M. R. de Oliveira, W. C. de Andrade Pereira, G. T. de Paula, and J. R. B. de Almeida Monteiro, "Optimized current waveform for torque ripple mitigation and MTPA operation of PMSM

with back EMF harmonics based on genetic algorithm and artificial neural network," *IEEE Latin America Transactions*, vol. 18, no. 09, pp. 1646–1655, 2020.
(28) G. Rigatos, M. Abbaszadeh, and P. Siano, "A nonlinear optimal control approach for permanent magnet ac motors with non-sinusoidal back emf," *Electrical Engineering*, pp. 1–26, 2022.
(29) J. Qu, C. Zhang, J. Jatskevich, and S. Zhang, "Deadbeat harmonic current control of permanent magnet synchronous machine drives for torque ripple reduction," *IEEE Journal of Emerging and Selected Topics in Power Electronics*, vol. 10, no. 3, pp. 3357–3370, 2021.
(30) W. Zhang and H. Bai, "Pmsm speed active disturbance rejection control based on modified extended state observer," *IEEJ Transactions on Electrical and Electronic Engineering*, p. e24114, 2024.
(31) M. Huang, Y. Deng, H. Li, and J. Wang, "Torque ripple suppression of PMSM using fractional-order vector resonant and robust internal model control," *IEEE Transactions on Transportation Electrification*, vol. 7, DOI 10.1109/TTE.2021.3053063, no. 3, pp. 1437–1453, 2021.
(32) P. P. Das, S. Satpathy, and S. Bhattacharya, "A voltage injection-based current harmonics suppression strategy for six-phase pmsm with nonsinusoidal back emf," *IEEE Journal of Emerging and Selected Topics in Industrial Electronics*, vol. 5, DOI 10.1109/JESTIE.2023.3337724, no. 1, pp. 285–297, 2024.
(33) L. R. Rocha, E. C. Silva, P. H. A. Silva, G. X. Prestes, B. C. R. Cordeiro, L. F. Pessoa, and R. P. Vieira, "Evaluation methodology of current control techniques for torque ripple reduction in non-sinusoidal PMSM," in *2023 IEEE 8th Southern Power Electronics Conference (SPEC)*, pp. 1–7. IEEE, 2023.
(34) D. M. C. Milbradt, G. V. Hollweg, P. J. D. O. Evald, and H. A. Gründling, "A robust adaptive one sample ahead preview controller for grid-injected currents of a grid-tied power converter with an LCL filter," *Int. J. of Elect. Power & Energy Systems*, vol. 142, p. 108286, 2022.
(35) G. V. Hollweg, P. J. D. O. Evald, D. M. C. Milbradt, R. V. Tambara, and H. A. Gründling, "Lyapunov stability analysis of discrete-time robust adaptive super-twisting sliding mode controller," *International Journal of Control*, vol. 96, no. 3, pp. 614–627, 2023.
(36) P. J. D. de Oliveira Evald, G. V. Hollweg, R. V. Tambara, and H. A. Gründling, "Lyapunov stab. analysis of a robust model reference adaptive PI controller for systems with matched and unmatched dynamics," *Journal of the Franklin Institute*, vol. 359, no. 13, pp. 6659–6689, 2022.
(37) L. Michels, R. De Camargo, F. Botteron, H. Grüdling, and H. Pinheiro, "Generalised design methodology of second-order filters for voltage-source inverters with space-vector modulation," *IEE Proceedings-Electric Power Applications*, vol. 153, no. 2, pp. 219–226, 2006.
(38) G. V. Hollweg, P. J. D. de Oliveira Evald, E. Mattos, L. C. Borin, R. V. Tambara, and V. F. Montagner, "Self-tuning methodology for adaptive controllers based on genetic algorithms applied for grid-tied power converters," *Control Engineering Practice*, vol. 135, p. 105500, 2023.
(39) G. V. Hollweg, P. J. D. d. O. Evald, E. Mattos, L. C. Borin, R. V. Tambara, and V. F. Montagner, "Optimized parametrization of adaptive controllers for enhanced current regulation in grid-tied converters," *International Journal of Adaptive Control and Signal Processing*, vol. 38, no. 1, pp. 200–220, 2024.
(40) Y. Zhao and J. Han, "Offline supervised learning vs online direct policy optimization: A comparative study and a unified training paradigm for neural network-based optimal feedback control," *Physica D: Nonlinear Phenomena*, vol. 462, p. 134130, 2024.
(41) K. S. Narendra, *Adaptive and learning systems: theory and applications*. Springer Science & Business Media, 2013.

Guilherme Vieira Hollweg (Non-member) received the B.Sc, M.Sc., and Ph.D. degrees in electrical engineering from the Federal University of Santa Maria (UFSM), Santa Maria, Brazil, in 2016, 2019, and 2021, respectively. He is currently an Assistant Professor at University of Michigan-Dearborn, Dearbon, MI, USA. He is also an IEEE-HKN member and faculty advisor for the UM-Dearborn Theta Tau Chapter. His research interests include control theory and applications, power electronics and motor drives control, optimization algorithms and renewable energy systems.

Lucas Rossato Rocha (Non-member) received the B.S., M. Sc. and the Ph.D. degrees in Electrical Engineering from Federal University of Santa Maria (UFSM) - Brazil in 2019, 2021, and 2025, where he is currently a postdoctorate researcher as a member of the Power Electronics and Control Group (GEPOC) and a lecturer in the Mechanical Eng. Department at UFSM. Dr. Rocha's main research interests include control and drive of electrical motors, control of non-sinusoidal PMSM, design and analysis of observers and study of control techniques to mitigate torque ripple in non-sinusoidal PMSM.

Van-Hai Bui (Non-member) received the B.E. degree from the Hanoi University of Science and Technology, Hanoi, Vietnam, in 2013, and the Ph.D. degree from Incheon National University, Incheon, South Korea, in 2020, both in electrical engineering. He is currently a Research Investigator and a Lecturer with the Department of Electrical and Computer Engineering, University of Michigan–Dearborn, Dearborn, MI, USA. His research interests include energy management systems, applications of reinforcement learning in smart grids, and microgrid operation.

Rodrigo Padilha Vieira (Non-member) received the B.S. degree in electrical engineering from the Universidade Regional do Noroeste do Estado do Rio Grande do Sul, Ijuí, Brazil, in 2007 and the M.Sc. and Ph.D. degrees in electrical engineering from the Federal University of Santa Maria (UFSM), Santa Maria, Brazil, in 2008 and 2012, respectively. From 2010 to 2014, he was with the Federal University of Pampa, Alegrete, Brazil. Since 2014, he has been with the UFSM, where he is currently a Professor. His research interests include electrical machine drives, sliding-mode control, and digital control of static converters.

Mengqi Wang (Non-member) received the B.S. degree from Xi'an Jiaotong University, Xi'an, China, in 2009, and the Ph.D. degree from North Carolina State University, Raleigh, NC, USA, in 2014, both in electrical engineering. She is currently an Associate Professor with the Department of Electrical and Computer Engineering, University of Michigan–Dearborn, Dearborn, MI, USA. Her research interests include dc–dc and dc–ac power conversions, high-efficiency and high-power-density power supplies, renewable energy systems, and wide-bandgap power device applications.

Wencong Su (Non-member) received the B.S. degree (Hons.) from Clarkson University, Potsdam, NY, USA, in 2008, the M.S. degree from Virginia Tech, Blacksburg, VA, USA, in 2009, and the Ph.D. degree from North Carolina State University, Raleigh, NC, USA, in 2013. He is currently a Professor and the Department Chair of Electrical and Computer Engineering with the University of Michigan-Dearborn, Dearborn, MI, USA. His research interests include power systems, transportation electrification, machine learning applications, and cyber-physical systems. He is a fellow of IET. He was a recipient of the 2015 IEEE Power and Energy Society Technical Committee Prize Paper Award and the 2013 IEEE Ind. Electronics Society (IES) Student Best Paper Award. He is an Editor of IEEE Trans. on Smart Grid and IEEE Power Eng. Letters. He is an Associate Editor of IEEE Access and IEEE Dataport.